Microporous and Mesoporous Materials 272 (2018) 286–295

Contents lists available at ScienceDirect

Microporous and Mesoporous Materials

journal homepage: www.elsevier.com/locate/micromeso

Direct wet deposition of zeolite FAU thin films using stabilized colloidal suspensions

Pei-Sun Huang [a], Chien-You Su [b], Chon Hei Lam [a], Wen-Ya Lee [c], Da-Ming Wang [a], Chi-Chung Hua [b, *], Dun-Yen Kang [a, **]

[a] Department of Chemical Engineering, National Taiwan University, Taipei 10617, Taiwan, ROC
[b] Department of Chemical Engineering, National Chung Cheng University, Chia-Yi 62102, Taiwan, ROC
[c] Department of Chemical Engineering and Biotechnology, National Taipei University of Technology, Taipei 10608, Taiwan, ROC

ARTICLE INFO

Article history:
Received 7 July 2017
Received in revised form
10 August 2017
Accepted 16 August 2017
Available online 18 August 2017

Keywords:
Zeolite FAU
Zeolite thin film
Wet deposition
Colloidal suspension

ABSTRACT

Seeded growth is the most popular approach to the preparation of zeolite thin films and membranes. Herein, we report a simplified method of fabricating zeolite Faujasite (FAU) thin films through the direct wet deposition of zeolite FAU thin films using stabilized colloidal suspensions. Zeolite FAU suspensions are stabilized by adjusting the pH values and the suspensions are spin-coated on a silicon wafer substrate to form dense zeolite FAU thin films. Dynamic light scattering (DLS) was used to investigate the colloidal properties of the zeolite FAU suspensions. The time-dependent hydrodynamic radius R_h was derived from DLS measurements for use as a quantitative measure of colloidal stability. It was found that high pH values destabilize the colloidal suspensions. Thin film samples cast using the relatively stable zeolite FAU suspensions yielded thin films with uniform morphology. In thin films formed from suspensions with a high pH value, the zeolite FAU crystals transformed into a dense phase. We also measured the relative permittivity (ε_r) of the thin film samples cast from various suspensions. At a low frequency (<100 kHz), thin films that compose zeolite FAU crystals presented higher ε_r values than did those possessing nonporous particles. The high ε_r values of the zeolite FAU thin films can probably be attributed to the physical adsorption of water. At a high frequency (1000 kHz), water had far less effect on ε_r values and thin films with a zeolite FAU structure presented ε_r values characteristic of low-dielectric constant (low-k) thin films.

© 2017 Elsevier Inc. All rights reserved.

1. Introduction

Zeolites are microporous crystalline aluminosilicates. Their well-defined micropore topology, tunable surface functionality, and high stability have led to the application of zeolites in catalysis [1], molecular separation [2,3], and water treatment [4,5]. Developments in the fabrication of zeolite membranes and thin films have opened up opportunities for the further application of zeolites. Zeolite membranes grown on a porous substrate can be used to facilitate separation processes in the chemical industry. Zeolite NaA (LTA framework type) membranes have been prepared for the industrial dehydration of ethanol and acetonitrile [6,7]. Zeolite DDR [8] and SAPO-34 [9] (CHA framework type) membranes have been used for CO_2/CH_4 separation with high selectivity of 220 at 301 K and 67 at 297 K respectively. Zeolite MFI membranes have also been used in desalination [10] as well as the separation of *p*-xylene and *o*-xylene produced in a membrane reactor [11]. Zeolite thin films deposited on a dense substrate can be used in microelectronics devices. Zeolite thin films have also been used to host dye molecules for use in humidity sensors [12,13]. Zeolite FAU cast on a quartz crystal has been used for sensing SO_2 [14], and various types of zeolite thin film have been fabricated for use as low-k thin films [15–19].

The application of zeolite membranes and thin films has followed developments in fabrication techniques [20–22]. Four main deposition techniques are available for the preparation of pure zeolite thin films/membranes: *in situ* crystallization, seeded growth, dry gel conversion, and direct deposition using a colloidal suspension. *In situ* crystallization refers to the immersion of a bare substrate in a zeolite growth solution, wherein the nucleation,

* Corresponding author.
** Corresponding author.
E-mail addresses: chmcch@ccu.edu.tw (C.-C. Hua), dunyen@ntu.edu.tw (D.-Y. Kang).

http://dx.doi.org/10.1016/j.micromeso.2017.08.031
1387-1811/© 2017 Elsevier Inc. All rights reserved.

growth, and intergrowth of crystals on the substrate all occur in the same step [23–25]. This method is limited by a long synthesis period (typically more than 2 days), which can have a profound effect on the quality of the membrane and supports [26]. Seeded growth is the most popular and reliable method for the fabrication of zeolite films/membranes. Seeded growth is a two-stage process in which zeolite crystals are first deposited on a bare substrate in a discrete form referred to as the seed layer [27–29]. The same substrate is then immersed in the growth solution to enable the secondary growth of the seed crystals, resulting in a continuous thin film/membrane. Dry gel conversion for the fabrication of zeolite films is similar to *in situ* crystallization, except that the substrate hangs in the air instead of being immersed in the growth solution. The vapor from the growth solution carries zeolite precursors, which crystallize as zeolites when they come into contact with the surface of the substrate [30–32]. All three of these methods can be used to produce zeolite thin films/membranes at the laboratory scale; however, industrial-scale production poses a number of serious challenges. These limitations have driven the development of methods for the direct deposition of zeolite thin films/membranes using colloidal suspensions. This method involves the casting of a stabilized zeolite suspension on a substrate *via* spin-coating or spray-coating. Unlike *in situ* crystallization, seed growth, or dry gel conversion, the direct deposition of zeolite thin films using colloidal suspensions often results in thin films in the absence of intergrown zeolite crystals. Thus zeolite thin films prepared *via* typical direct deposition are not ideal for molecular sieving, but they can be well applied as low-*k* dielectric layer.

The successful deposition of zeolite films using a colloidal suspension depends on the stability of the suspension, the use of small crystals, and the inclusion of an appropriate surfactant. Uniform thin films have been fabricated by spin-coating pure silica zeolite MFI suspensions with crystals of 37 nm synthesized over a period of 36 h. Synthesizing the same material over a longer period (48 h) resulted in larger crystals (60 nm), which produced thin films of poor quality [33]. The addition of an non-ionic surfactant, such as TWEEN® 80, is crucial to the preparation of high-quality thin films of pure silica zeolite MFI through the direct deposition of a colloidal suspension [34]. Thin films comprising zeolite MFI [35,36], MEL [37,38], BETA [39], $AlPO_4$-18 [40], ZSM-2 [41], NaA [42], and BEA [43] have been successfully prepared using this approach. The physical properties of zeolite colloidal suspensions have been investigated using dynamic light scattering (DLS), small-angle X-ray scattering (SAXS), high-resolution transmission electron microscopy (HR TEM), NMR and zeta potential [44–47]. However, few reports have addressed the relationship between the colloidal properties of zeolite suspensions and thin film deposition [48–52]. In particular, it has been found that the surface charge [51,52] as well as the crystal size [48,51] in the colloidal suspensions have great impact on the thin film quality. The radius of gyration of the zeolite colloids, determined *via* SAXS, has been known to have strong impact on the packing of zeolite particles in solid state, which affects the thin film porosity [49].

In this paper, we report on the fabrication of zeolite FAU thin films using direct wet deposition of stabilized colloidal suspensions. Our primary aim was to elucidate the relationships between the colloidal properties of zeolite suspensions and thin film deposition. In particular, effects of pH and surfactant added in the cast solutions on the microstructure of resulting thin films were discussed. Suspensions containing zeolite FAU (Si:Al = 50:7) nanocrystals with or without the surfactant TWEEN® 80 at various pH values were used in this study. Nanocrystals were imaged using transmission electron microscopy (TEM). Quantitative analysis on the colloidal suspensions was performed using DLS. The zeolite FAU suspensions were spun-cast on silicon wafer substrates and then calcined to form solid-state thin films. The thin film morphology, as characterized using optical microscopy (OM) and scanning electron microscopy (SEM), was correlated to the results from DLS analysis. The relative permittivity of the thin films was measured to evaluate their applicability as dielectric thin films.

2. Experimental

2.1. Materials

Sodium hydroxide (NaOH, 97%, pellets), colloidal silica (Ludox HS-30, 30 wt. % SiO_2 in H_2O (pH = 9.8)), and polysorbate 80 (TWEEN® 80, viscous liquid) were purchased from Sigma-Aldrich. Aluminum powder (325 mesh, 99.5%) was purchased from Alfa Aesar. All chemicals were used without further purification. Deionized water (DI water) used in the synthesis process was obtained using the ELGA™ PURELAB® Classic DI ultra-pure water system.

2.2. Preparation of zeolite FAU suspensions

Four types of zeolite FAU suspensions were prepared in this study. Synthesis was conducted in accordance with procedures outlined in a previous work with minor modifications [53]. Two separate solutions were prepared for synthesis. The first step involved dissolving 2 g of NaOH in 4 g of DI water in a bottle made of perfluoroalkoxy alkane (PFA) with a maximum capacity of 100 ml. To this mixture was slowly added 0.189 g of aluminum powder to form solution I. Solution II was prepared by mixing 10 g of colloidal silica, 1.6 g of NaOH, and 3.4 g of DI water in a 100 ml PFA bottle. The bottle was placed in an oven at 105 °C for 6 min until the solution became completely transparent, and then moved to an ice bath under vigorous stirring. Solution I was added dropwise to solution II. The mixture comprising solutions I and II had a molar ratio of 9 Na_2O: 0.7 Al_2O_3: 10 SiO_2: 160 H_2O and of a total mass of 21.189 g. The mixed solution was aged at 30 °C for 24 h, and then transferred to a Teflon-lined autoclave with a maximum capacity of 180 mL. The autoclave was placed in an oven at 50 °C for 45 h to form a stock solution containing zeolite FAU crystals for use in the preparation of four cast suspensions.

A total of 5 g of the stock solution was mixed with 5 g of DI water and then stirred at 30 °C for a period of 24 h to form cast suspension A. Cast suspension B was prepared similarly, but included 0.354 g of TWEEN® 80. Cast suspension C was produced by mixing 5 g of stock solution with 5 g of DI water, followed by centrifugation at 15,000 rpm for 20 min using a HERMLE Centrifuge Z 36 HK. The resulting supernatant was decanted, and fresh water was added to the precipitate until it reached a total mass of 10 g. The suspension was centrifuged again under the same conditions, and fresh water was again added to reach a total mass of 10 g. During this two-stage centrifugation process, the pH of the zeolite FAU suspension dropped from 13.5 to 12.5. The suspension underwent stirring at 30 °C for 24 h to form cast suspension C. Cast suspension D was prepared similarly to cast suspension C, but included 0.708 g of TWEEN® 80.

2.3. Characterization of suspensions

The morphology of zeolite FAU crystals in the suspension was examined using a Hitachi H-7100 transmission electron microscope (TEM) operated at an accelerated voltage of 75 kV.

Wide-angle X-ray scattering (WAXS) patterns of suspension samples were obtained in transmission mode using the facilities at beamline 23 A station at the National Synchrotron Radiation Research Center (NSRRC) in Taiwan. We employed incidence X-rays

with energy of 15 keV (0.8267 Å) and a sample-to-detector distance of 148.62 mm. Scattering patterns were recorded using a Flat Panel CMOS detector with exposure of 10 s.

Dynamic light scattering (DLS) measurements were obtained using a homemade multiple angle (30°–140°) light scattering apparatus as described in previous studies [54,55]. The instrument was equipped with a polarized He-Ne laser ($\lambda_0 = 632.8\ nm$; Lasos, LGK 7626S) and a Peltier thermal controller. Suspension samples of 2 mL were placed in a capped cylindrical quartz cell 1 cm in diameter (Hellma, 540.111, Germany). All measurements were conducted at 25±0.1 °C.

The physical quantity measured directly in the homodyne DLS experiment was the normalized intensity-time correlation function, $g^{(2)}(q,\ t)$, where t is the decay time and q the scattering vector. $q = 4\pi n sin(\theta/2)/\lambda_0$, where n is the refractive index of solvent, θ is the scattering angle, and λ_0 is the wavelength of incident light in a vacuum. The normalized electric field correlation function, $g^{(1)}(q,\ t)$, was derived from $g^{(2)}(q,\ t)$ using the Siegert relation: $g^{(2)}(q,\ t) = 1 + \beta|g^{(1)}(q,\ t)|^2$ [56], where β $(0<\beta<1)$ is the spatial coherence factor. The normalized electric field correlation function $g^{(1)}(q,\ t)$ can be related to the decay rate distribution using the Laplace transformation: $|g^{(1)}(q,\ t)| = \int_0^\infty G(\Gamma)exp(-\Gamma t)d\Gamma$, where the detailed distribution $G(\Gamma)$ was obtained using the inverse Laplace transformation and commercial software CONTIN [57]. From the decay rate distribution, the q-dependence of the mean decay rate, Γ, can be expressed as $\Gamma \sim q^\alpha$, where the scaling exponent is indicative of a specific relaxation mechanism (e.g. $\alpha = 2$ for diffusive motion).

It is convenient to describe suspension systems exhibiting a single diffusion mode, $g^{(1)}(t)$, using the cumulant expansion [58]: $g^{(1)}(t) = exp(-K_1 t + K_2 t^2/2 - K_3 t^3/6\cdots)$, where K_1 represents the mean decay rate, Γ, K_2 indicates the variance in size distribution, and K_3 reflects the skewness of the distribution [59]. The intensity-weighted average of the diffusion coefficient, D, can be calculated from $D = \Gamma/q^2$. Accordingly, the hydrodynamic radius, R_h, can be estimated using the Stokes-Einstein equation, $R_h = k_B T/6\pi\eta D$, where k_B is Boltzmann's constant, and η is the solvent viscosity measured at absolute temperature T.

2.4. Preparation of zeolite FAU powder

The cast suspensions were drop-cast on the silicon wafer and dried in an oven at 100 °C for 24 h to form powder samples. The powder samples were calcined in a furnace by raising the temperature to 550 °C at an elevation rate of 1 °C per minute and then held at that temperature for 6 h. Following calcination, the solid-state film was scraped off the substrate and ground to form a powder. The powder sample derived from cast suspension A was referred to as powder A, and the remaining samples were named by analogy. Powders A, B, C and D were only used for nitrogen physisorption measurements.

2.5. Characterization of powder

Nitrogen physisorption was performed at 77 K using a Micromeritics ASAP 2020 analyzer. Samples were degassed at 200 °C for 24 h prior to measurement.

2.6. Preparation of zeolite FAU thin films

Silicon wafers substrates were purchased from SUMMIT-TECH Resource Corp. The silicon wafers were P-boron type with native oxide and orientation of (100) +/-0.5° and resistivity of 1.5–100 ohm-cm. The wafers were cut into squares (approximately 2 × 2 cm) for use as substrates. Cast suspensions A, B, C, D were separately spin-cast on the substrate at various spin rates (1000, 2000, or 3000 rpm) for a period of 30 s using a spin-coater (Laurell Model-WS-650M2-23NPPB). The samples were placed in a drying oven and baked at 100 °C for 24 h. They were then moved to a furnace where the temperature was increased to 550 °C at an elevation rate of 1 °C per minute and then held at that temperature for 6 h. The thin film derived from cast suspension A spun at 1000 rpm was referred to as thin film A (1000 rpm), and the remaining samples were named by analogy.

2.7. Characterization of thin films

X-ray diffraction (XRD) was performed on the powder scrapped off from the thin film samples using a PANalytical X'pert diffractometer operated with a Cu Kα source, scanning from 5° to 40° 2θ with a step size of 0.02°.

Top-view and side-view images of the thin films were recorded using a scanning electron microscope (FEI Nova NanoSEM™ 230) operated at a primary energy of 5 keV under pressure of 5×10^{-6} Torr in the specimen chamber. A thin layer of platinum was deposited on the samples prior to imaging.

An optical microscope (Whited WM-100) was used to image the thin film samples as well as the solutions spun-cast on the substrates.

Physical vapor deposition (PVD) was used to fabricate gold electrodes on the thin films for the measurement of capacitance. The pressure in the vacuum chamber was first lowered to less than 10^{-5} torr. A rotary table (operating at 10 rpm) was used for the placement of samples. The operating current of the gold heater was 65 A, resulting in a gold deposition rate of 0.9 Å/s. The final thickness of the gold electrode was 100 nm. Capacitance was measured using a Keysight 4284 A Precision LCR meter under a bias voltage of 1 V. Measurements were conducted at frequencies of 1, 10, 100, and 1000 kHz. The relative permittivity (ε_r) of the thin films was calculated using the relation $\varepsilon_r = Cd/\varepsilon_0 A$, where C is the measured capacitance, d is the thickness (determined from cross-sectional SEM images), A is the area of the deposited electrode (2 mm^2), and ε_0 is the vacuum permittivity (8.85×10^{12} F/m).

3. Results and discussion

Fig. 1 presents photographic images of cast suspensions A, B, C, and D. The four suspensions had the same zeolite to water mass ratio. Cast suspensions A and B had a pH value of 13.5, whereas cast suspensions C and D had a pH value of 12.5. The surfactant, TWEEN® 80, was included only in suspensions B and D. All four of the zeolite FAU suspensions presented signs of good dispersion immediately after agitation (Fig. 1a). Severe precipitation was observed in cast suspensions A, B, and D after sitting for 24 h. Even after 24 h, cast suspension C maintained relatively good dispersion, indicating that a low pH value is beneficial to the dispersion of FAU nanocrystals in aqueous phase. Counter-intuitively, the surfactant appears to have had a negative impact on the dispersion of zeolite FAU particles. A previous study reported that this surfactant greatly enhances the dispersion of pure silica zeolite MFI and amorphous silica nanoparticles in water. The differences in these findings are likely due to trace amounts of aluminum doping in the zeolite FAU (Si:Al = 50:7) used in this study.

Fig. 2 presents transmission electron microscopic (TEM) images of the four suspensions, indicating that all of the zeolite FAU crystals were on the scale of tens of nanometers, regardless of their pH value or the presence of surfactant. Cast suspensions A and B exhibited stronger aggregation than did the other two suspensions, which is in agreement with the macroscopic observations described in the preceding section. Cast suspension D showed

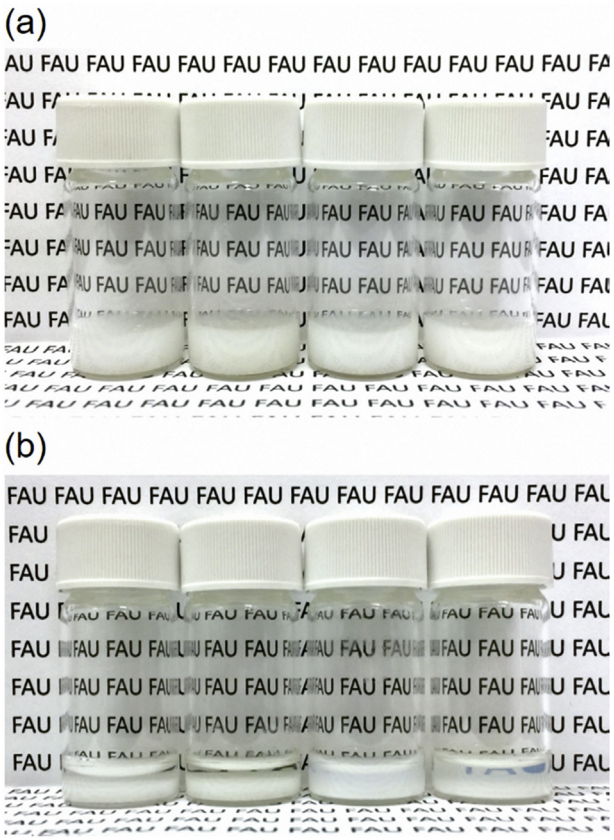

Fig. 1. Photographs of cast suspensions: (a) stirring for 24 h, (b) standing for 24 h; from left to right are cast suspensions A, B, C, D, respectively.

slightly less aggregation than did cast suspension C, which may be attributed to the presence of TWEEN® 80 in suspension D. This finding appears to contradict the results of sedimentation tests discussed above. Thus, we employed dynamic light scattering (DLS) to gain further insight into these four zeolite FAU suspensions.

DLS analysis has been used widely to investigate the time evolution of zeolite particle size during nucleation or aggregation [60–62]. In this study, DLS measurements were performed on pristine suspensions as well as diluted samples. Typical DLS analysis cannot be applied directly to pristine samples due to the possibility of multiple scattering; however, the general features are still useful in revealing major differences between the four cast suspensions. Fig. 3 presents the $g^{(1)}(q, t)$ curves for the pristine suspension samples. The curves for suspensions that underwent centrifugation (C and D) were remarkably smoother than those that did not undergo this treatment (A and B). This is an indication that suspensions C and D were more homogeneous or more effectively stabilized than were suspensions A and B.

To obtain more detailed, quantitative analysis of the underlying particulate state of the individual suspensions, we diluted the pristine suspensions by a factor of 40 using DI water. Fig. 4 presents a comparison of the DLS measurement results. Diluting the samples (without further filtration) minimized the impact of multiple scattering, thereby enabling the adoption of the analysis schemes introduced earlier. The four suspensions exhibited a single diffusion mode (i.e., the results from four scattering angles were superposed on the same curve after decay time t had been rescaled using q^2), suggesting there were no appreciable contributions from species (such as dust particles) other than the FAU particles themselves. The corresponding hydrodynamic radius, R_h, was noticed to fluctuate with aging time. Thus, we monitored the time-dependent R_h of each suspension sample at a small scattering angle of 30° within a period of 80–100 min, as shown in Fig. 5. All of the R_h values

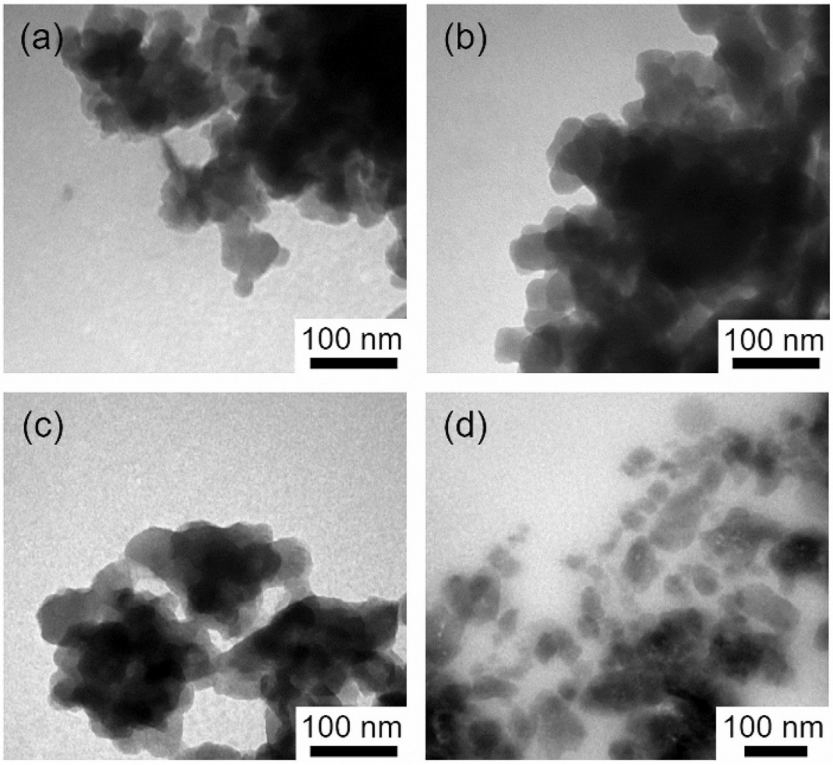

Fig. 2. TEM images of cast suspensions (a) A, (b) B, (c) C, and (d) D.

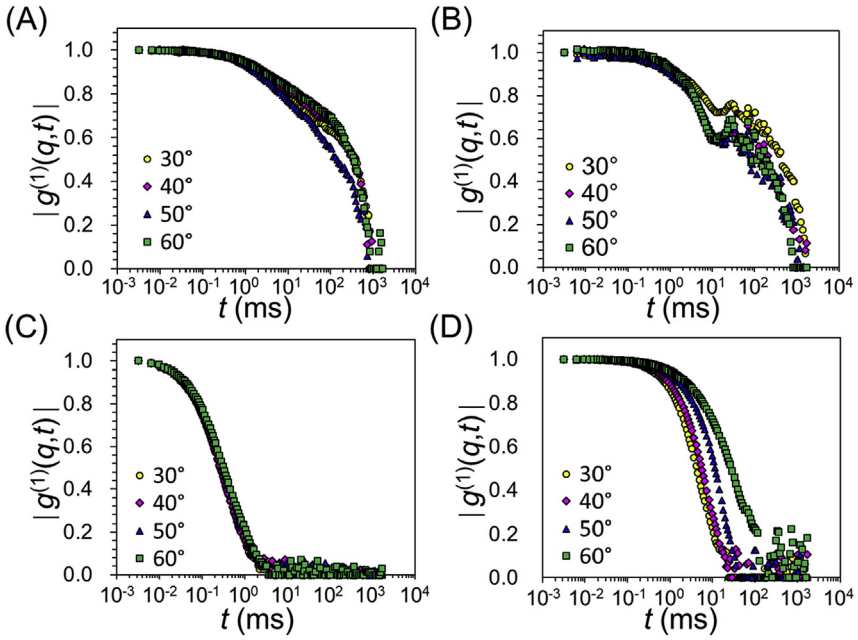

Fig. 3. Field correlation functions of pristine zeolite FAU suspensions: (a) A, (b) B, (c) C, and (d) D.

obtained from the suspension samples (cf. suspension A: 193 ± 49 nm; B: 400 ± 240 nm; C: 292 ± 29 nm; D: 347 ± 68 nm) fell between 200 and 400 nm, which is ideal for applications involving microporous materials [63]. Suspensions C and D presented lower standard deviation than did suspensions A and B over the monitored time span. This is an indication that suspensions C and D were more stable than suspensions A and B.

From the observations above, the effects of centrifugation treatment and TWEEN® 80 addition seem evident. Specifically, suspensions C and D (with centrifugation treatment, pH = 12.5) showed less fluctuation in R_h with aging time than did suspensions A and B (without centrifugation treatment, pH = 13.5). This is an indication that zeolite FAU suspensions are more stable at a lower pH. Moreover, suspension B (in the presence of TWEEN® 80) presented the greatest fluctuation in R_h, which suggests that the surfactant TWEEN® 80 tends to destabilize (rather than stabilize) the suspension. Overall, the DLS characteristics observed in the pristine suspension samples and the (time-dependent) behavior of R_h for their diluted counterparts lead to conclusions consistent with those obtained in sedimentation tests and TEM characterization. Namely, a higher pH value or the addition of TWEEN® 80 destabilizes zeolite FAU suspensions. In a later discussion, we show how the colloidal properties of these suspensions influence the morphology of the resulting thin films.

Four zeolite FAU suspensions were used for thin film deposition *via* spin-coating at three spin rates (1000, 2000, and 3000 rpm),

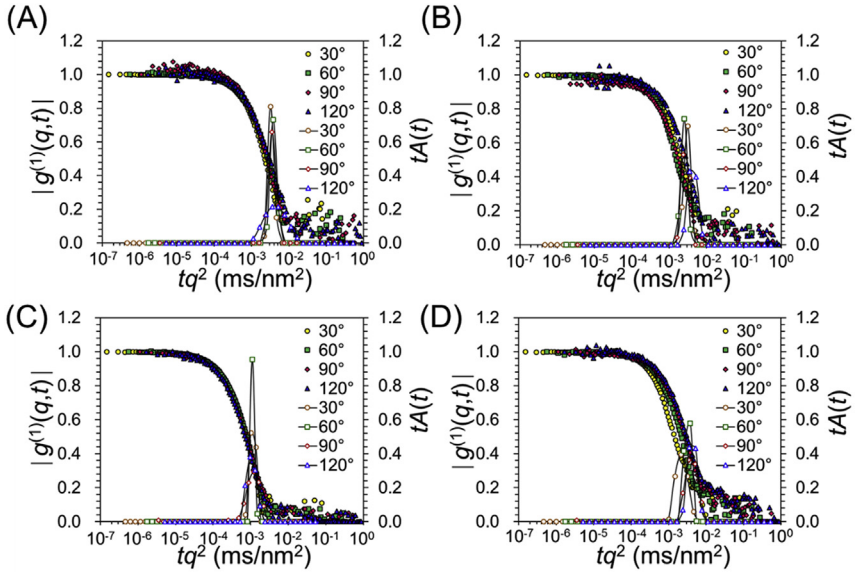

Fig. 4. Angular dependences of field correlation function and associated decay time distribution extracted from CONTIN for zeolite FAU suspensions (a) A, (b) B, (c) C, and (d) D. These suspensions were pristine suspension samples diluted by a factor of 40 and decay time t has been rescaled using q^2.

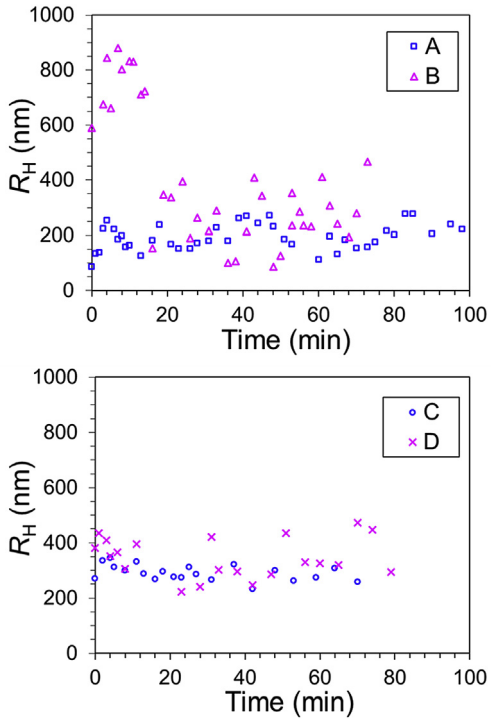

Fig. 5. Time-dependent behavior of R_h for suspensions A, B, C, and D. These suspensions were pristine suspension samples diluted by a factor of 40.

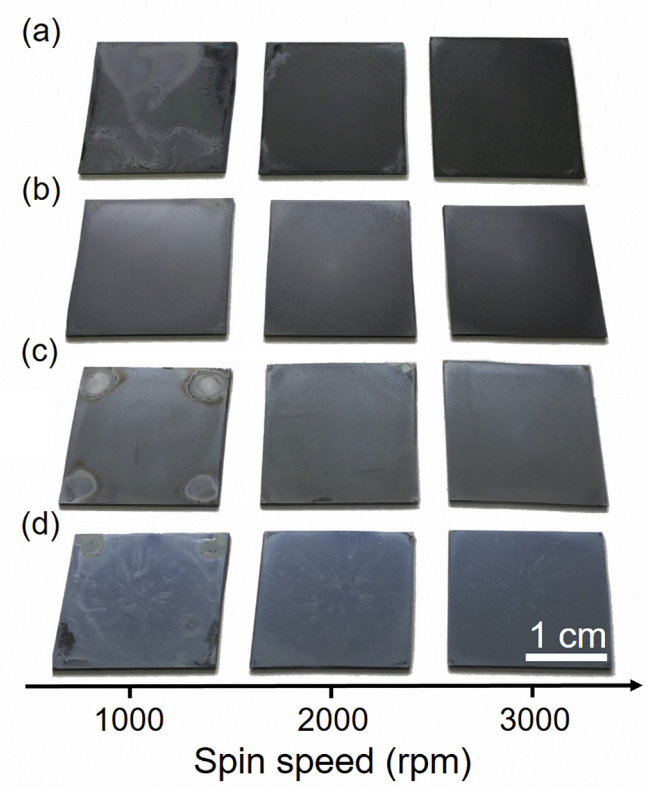

Fig. 6. Photographs of (a) thin film A, (b) thin film B, (c) thin film C, and (d) thin film D cast at various spin rates.

which resulted in 12 thin film samples. Silicon wafers with a thin layer of native oxide were used as substrates. The thin film derived from cast suspension A spun at 1000 rpm was referred to as thin film A (1000 rpm), and the remaining samples were named by analogy. We first examined the macroscopic morphology of the thin film samples using photographic images (Fig. 6). Thin films A, B, C, and D spun at 1000 rpm were less uniform than the samples spun at higher rates. Cast suspension B was identical to suspension A except for the addition of TWEEN® 80 in suspension B. Nonetheless, no noticeable difference was observed between thin film A (2000 rpm) and thin film B (2000 rpm). Furthermore, thin film A (3000 rpm) and thin film B (3000 rpm) were almost identical with regard to uniformity. The only difference between cast suspensions C and D was the presence of surfactant in suspension D. Radial patterns were observed in thin film D (2000 rpm) as well as thin film D (3000 rpm), whereas the surface morphology of thin film C (2000 rpm) and thin film C (3000 rpm) were relatively uniform at the millimeter scale. This is a clear indication that TWEEN® 80 had a negative effect on the wet deposition of zeolite FAU thin films.

Fig. 7 presents a top-view optical microscopic (OM) image of the 12 thin film samples. Unlike the observations obtained from photographic images at the millimeter scale, the surface morphology at the scale of hundreds of micrometers appeared unaffected by the spin rate. Thin film A showed the highest surface roughness, regardless of the spin rate (1000, 2000, and 3000 rpm). The surface roughness of thin films B (spun at all rates) was slightly lower than that of thin film A. The surface morphology of thin films C and D (spun at all rates) was smooth at the scale of hundreds of micrometers. The morphological characteristics obtained using OM demonstrated that reducing the pH value (from 13.5 to 12.5) of the cast suspension resulted in thin films of greater smoothness. We also investigated the top-surface morphology of the thin film samples using scanning electron microscopy (SEM). These images can be found in the *Supplementary Information* (Fig. S1). Our surface roughness results from SEM characterization are nearly identical to those obtained through OM investigation. The results of morphology characterization can be rationalized by the results from the DLS analysis in the preceding section, wherein low-pH suspensions (suspensions C and D) are more stable than high-pH

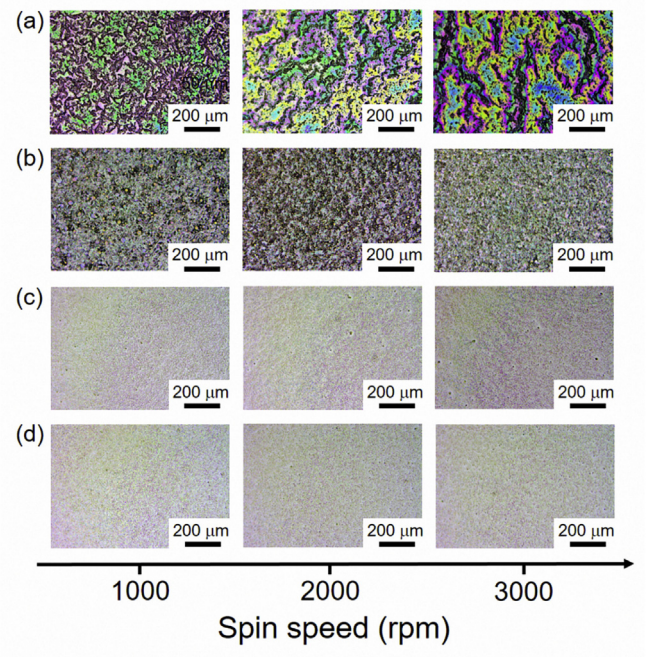

Fig. 7. OM images of (a) thin film A, (b) thin film B, (c) thin film C, and (d) thin film D cast at various spin rates.

suspensions (suspensions A and B), such that low-pH suspensions produce thin films of greater uniformity. Nonetheless, despite the fact TWEEN® 80 also destabilized the suspension (as indicated by DLS analysis), this was shown to have negligible effects on the morphology of the thin films.

Fig. 8 shows cross-sectional SEM images of the 12 thin film samples. The thickness of thin films A and B was shown to decrease with spin rate. The average thicknesses were as follows: thin film A (1000 rpm), thin film A (2000 rpm), and thin film A (3000 rpm) were approximately 1.3, 1.2, and 0.8 μm respectively. The average thickness of thin film B (1000 rpm), thin film B (2000 rpm), and thin film B (3000 rpm) were approximately 1.0, 0.95, and 0.8 μm respectively. Interestingly, the thickness of thin films C and D appear to be unaffected by spin rate: all samples of thin films C and D possessed an average film thickness of approximately 600–700 nm. The cross-sectional morphology of thin films A and B is also distinct from that of thin films C and D. Specifically, voids of several micrometers were present in thin films A and B but absent from thin films C and D. Void formation was likely related to phase transformation during the wet deposition of thin films A and B. This issue is discussed in the subsequent section on characterization by X-ray diffraction.

In order to better understand the effects of pH of the cast suspensions on the resulting thin films, the cast suspensions at pH = 3, 7, and 10 were prepared and cast to form films. It was found that the suspensions at pH = 10 and 12.5 were most stabilized, and severe sedimentation was found in the suspensions at pH = 3 and 13.5 (*Supplementary Information*, Fig. S2). The thin films formed using the cast suspension at pH = 10 and 12.5 also possessed uniform surface, as compared to those formed using the cast suspensions at pH = 3, 7, and 13.5 (*Supplementary Information*, Figs. S3 and S4). The results suggest that the weak basic environment are beneficial to the thin film formation of zeolite FAU with Si:Al = 50:7. This might be explained by the fact that the zeolite crystals discussed in this work possess surface charges in a weak basic environment, and this causes repulsive force among particles. A similar finding about pH effects on the surface charges of zeolites has been reported previously, in which they found silicalite-2 crystals with surface charges (at pH = 3 or 10) in the suspension resulted in better-quality thin films [52,64] as compared to suspensions at pH = 7.

It was previously reported that different synthesis schemes and preparation procedures can result in similar particle size distributions but with variations in the crystallinity of FAU-type suspensions [65]. The thin film samples underwent characterization using X-ray diffraction (XRD) to shed light on the underlying crystallinity. The XRD patterns of thin films spun at 1000 rpm are presented in Fig. 9a. Overall, the XRD patterns were unaffected by the spin rate but were affected by the pH value of the cast suspension. Specifically, thin films C and D (derived from cast suspensions with pH = 12.5) presented XRD patterns indicating the presence of zeolite FAU phase. However, the XRD patterns of thin films A and B (from cast suspensions with pH = 13.5) indicate the absence of zeolite FAU phase and the presence of a distinct crystalline phase. This distinct crystalline phase is very likely to be fused fly ash [66], which is composed of crystalline aluminosilicate and sodium silicate (*Supplementary Information*, Fig. S5). We hypothesize that the zeolite FAU phase was present in pristine cast suspensions A and B; however, the increase in pH value during the baking process due to the evaporation of solvent led ultimately to the destruction of the zeolite FAU crystals, such that it transformed into a distinct phase.

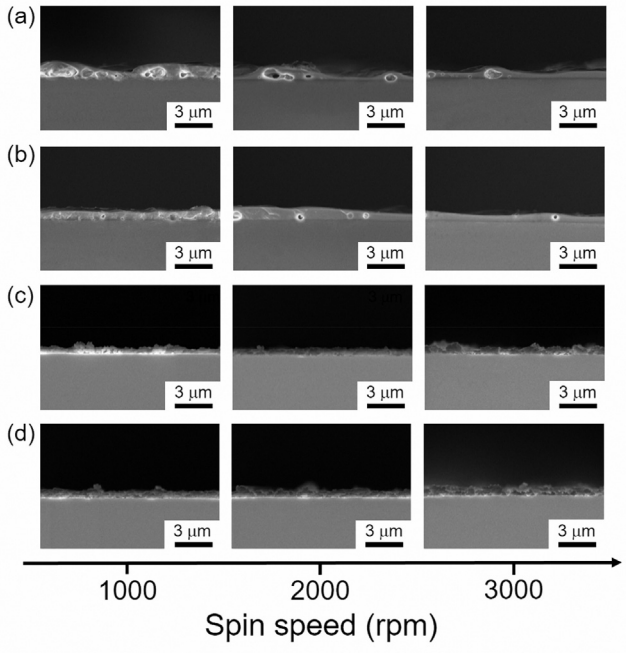

Fig. 8. Side-view SEM images of (a) thin film A, (b) thin film B, (c) thin film C, and (d) thin film D cast at various spin rates.

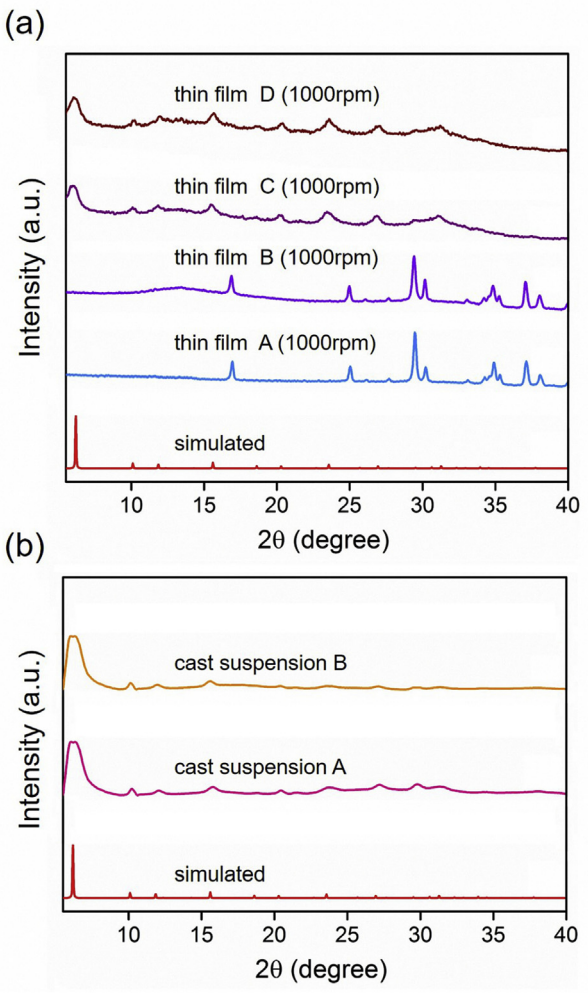

Fig. 9. (a) XRD patterns of thin film samples, (b) XRD pattern of powder C and 1D WAXS patterns of suspension A and B derived from raw 2D WAXS patterns. Simulated XRD patterns of zeolite FAU are included in (a) and (b).

To test this hypothesis, we employed transmission-mode wide-angle X-ray scattering (WAXS) to examine cast suspensions A and B. The raw 2D WAXS patterns are presented in the *Supplementary Information* (Fig. S6), and the deduced 1D WAXS patterns are presented in Fig. 9b. The crystals in cast suspensions A and B both presented the characteristic diffraction patterns of zeolite FAU. This suggests that zeolite FAU crystals did exist in the cast suspensions A and B (with pH value of 13.5). To further investigate the phase transformation of zeolite FAU during the drying of cast suspensions A and B, we conducted nitrogen physisorption tests on four samples of powder obtained by drying cast suspensions A, B, C, and D (*Supplementary Information*, Fig. S7). The nitrogen physisorption isotherms of powders C and D suggest that their microporosity can be attributed to the topology of zeolite FAU, whereas the meso/macroporosity is associated with the gaps between zeolite nanocrystals. In contrast, the nitrogen physisorption isotherms indicate that powders A and B were completely nonporous. This is consistent with the results derived from XRD, wherein zeolite FAU topology was shown not to exist in either powders A or B, or thin films.

It would be reasonable to expect that the difference in porosity and crystallinity among the various thin film samples would affect their dielectric properties, when serving as a dielectric thin film in electronic devices. Thus, we measured the relative permittivity (ε_r), also known as the dielectric constant, of thin films A, B, C, and D spun at 2000 and 3000 rpm (Fig. 10). At frequencies below 100 kHz, the relative permittivity of thin films A and B (with almost no porosity) presented relative permittivity far below that of thin films C and D. Zeolite FAU has been known as good water sorbent [67–69]. The relatively high porosity of thin films C and D, suggested by the results of nitrogen physisorption, resulted in capability of adsorbing water under ambient conditions. In contrast, thin films A and B, which do not possess zeolite FAU topology and are nonporous according to nitrogen physisorption, have low water adsorption capacity. Physically adsorbed water generally raises the relative permittivity of dielectric materials in the low frequency regime [70,71]. However, in the high frequency region, the contribution of the adsorbed water to relative permittivity is greatly reduced, such that the composition and the porosity of the materials tends to dominate. All of the thin film samples in this work have nearly identical compositions; therefore, those with higher porosity show lower relative permittivity. We found that at 1000 kHz, thin films C and D (relatively high porosity) presented a lower ε_r than did thin films A and B (Fig. 10c). When the applied frequency was 1000 kHz, the low relative permittivity of these eight thin film samples qualified them as low-*k* thin films ($\varepsilon_r < 4.0$) [72]. The relative permittivity of commercialized zeolite FAU measured in pallet form exhibited a relative permittivity of 18 at 1000 kHz [73]. It has also been reported that the relative permittivity of a zeolite FAU-PVDF composite is approximately 8 at 1000 kHz [74].

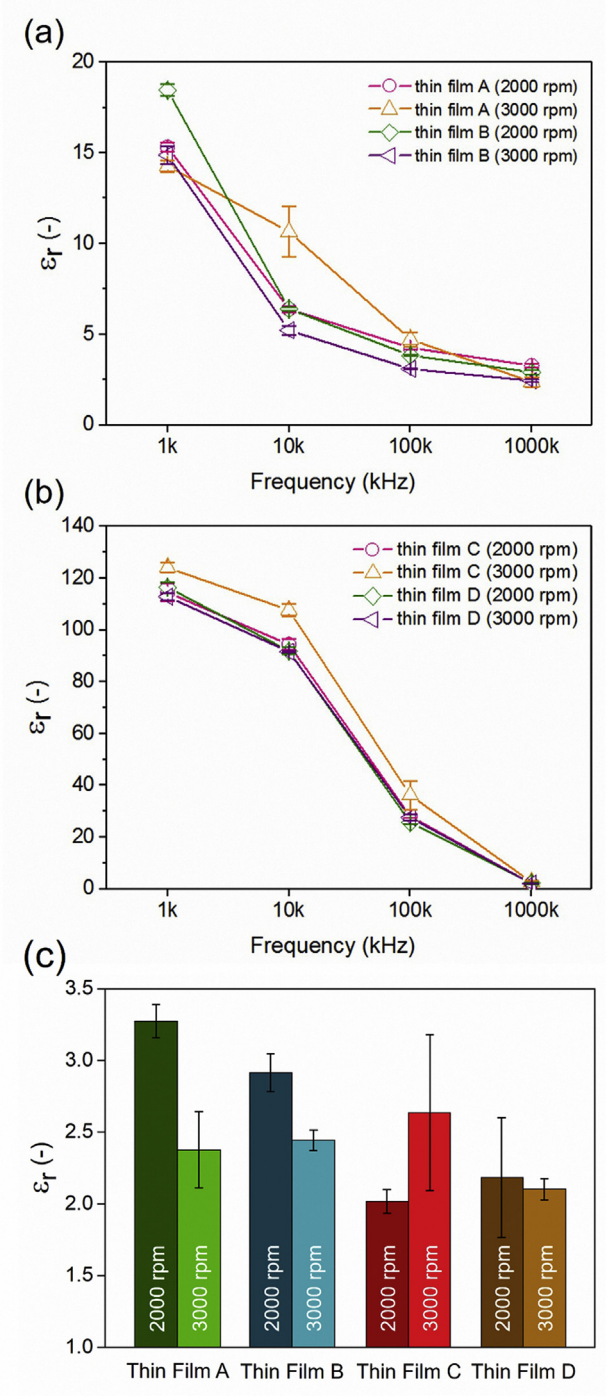

Fig. 10. Relative permittivity (dielectric constant) of (a) thin film A and B cast at various spin rates; (b) thin film C and D cast at various spin rates; (c) relative permittivity of thin film samples measured at high frequency (1000 kHz).

4. Conclusions

In this paper, we report on a new approach to the fabrication of zeolite FAU thin films through the direct wet deposition of zeolite FAU thin films using stabilized colloidal suspensions. Zeolite suspensions were prepared with pH values of 12.5 and 13.5. We then produced cast suspensions with and without the surfactant, TWEEN® 80, which were then cast on a silicon wafer substrate *via* spin-coating to form dense zeolite FAU thin films. TEM and DLS was applied to suspension samples to elucidate the relationship between the properties of the suspensions and those of thin films. The time-dependent hydrodynamic radius R_h derived from DLS measurements was used as a quantitative measure of colloidal stability. It was found that colloidal suspensions with a higher pH value (13.5) were less stable. Interestingly, the suspensions that included TWEEN® 80 were also less stable, which indicates that the surfactant destabilized the zeolite FAU suspensions. The thin film samples cast using relatively stable zeolite FAU suspension (pH = 12.5 without TWEEN® 80) yielded thin films with uniform morphology. Thin films formed from suspension at pH = 13.5 lost the zeolite FAU crystallinity due to the decomposition of crystals within a high-pH environment. According to the results of nitrogen physisorption,

the zeolite FAU crystals suspended in water at pH = 13.5 transformed into a dense phase after drying. We also measured the relative permittivity (ε_r) of the thin film samples cast from the various suspensions. At a low frequency (<100 kHz), thin films containing zeolite FAU crystals presented higher ε_r values than did the suspensions with nonporous particles. The high ε_r of the zeolite FAU thin films can probably be attributed to the physical adsorption of water. At a high frequency (1000 kHz), the contribution of water to ε_r far less pronounced. Thin films with a zeolite FAU structure showed ε_r values characteristic of low-dielectric constant (low-*k*) thin films. The wet deposition method reported in this study greatly simplifies the synthesis of zeolite thin films and membranes, thereby opening up new possibilities for the large-scale application of zeolite materials.

Acknowledgments

P.-S. Huang, C.-H. Lam, and D.-Y, Kang acknowledge the financial support from the Ministry of Science and Technology (MOST) of Taiwan (MOST 104-2628-E-002-009-MY3 and MOST 105-2221-E-002-056-MY2). C.-Y. Su and C.-C. Hua acknowledge the financial support from the Ministry of Science and Technology of Taiwan (MOST 103-2221-E-194-059-MY3). All of the authors acknowledge technical support from U-Ser Jeng, Chun-Jen Su, Yi-Qi Yeh, Chun-Yu Chen, Wen-Bin Su, and Kuei-Fen Liao at beamline 23 A in National Synchrotron Radiation Research Center of Taiwan. We also acknowledge the valuable assistance received from Chun-Chi Chen in the measurement of nitrogen physisorption.

Appendix A. Supplementary data

Supplementary data related to this article can be found at http://dx.doi.org/10.1016/j.micromeso.2017.08.031.

References

[1] A. Corma, From microporous to mesoporous molecular sieve materials and their use in catalysis, Chem. Rev. 97 (1997) 2373–2419.
[2] M. Ackley, Application of natural zeolites in the purification and separation of gases, Microporous Mesoporous Mater 61 (2003) 25–42.
[3] M. Tagliabue, D. Farrusseng, S. Valencia, S. Aguado, U. Ravon, C. Rizzo, A. Corma, C. Mirodatos, Natural gas treating by selective adsorption: material science and chemical engineering interplay, Chem. Eng. J. 155 (2009) 553–566.
[4] S. Wang, Y. Peng, Natural zeolites as effective adsorbents in water and wastewater treatment, Chem. Eng. J. 156 (2010) 11–24.
[5] A. Hedstrom, Ion exchange of ammonium in zeolites: a literature review, J. Environ. Eng. 127 (2001) 673–681.
[6] Y. Morigami, M. Kondo, J. Abe, H. Kita, K. Okamoto, The first large-scale pervaporation plant using tubular-type module with zeolite NaA membrane, Sep. Purif. Technol. 25 (2001) 251–260.
[7] D. Liu, Y. Zhang, J. Jiang, X. Wang, C. Zhang, X. Gu, High-performance NaA zeolite membranes supported on four-channel ceramic hollow fibers for ethanol dehydration, RSC Adv. 5 (2015) 95866–95871.
[8] T. Tomita, K. Nakayama, H. Sakai, Gas separation characteristics of DDR type zeolite membrane, Microporous Mesoporous Mater 68 (2004) 71–75.
[9] S. Li, SAPO-34 membranes for CO_2/CH_4 separation, J. Membr. Sci. 241 (2004) 121–135.
[10] M. Kazemimoghadam, T. Mohammadi, Synthesis of MFI zeolite membranes for water desalination, Desalination 206 (2007) 547–553.
[11] S. Haag, M. Hanebuth, G.T.P. Mabande, A. Avhale, W. Schwieger, R. Dittmeyer, On the use of a catalytic H-ZSM-5 membrane for xylene isomerization, Microporous Mesoporous Mater 96 (2006) 168–176.
[12] I. Pellejero, M. Urbiztondo, D. Izquierdo, S. Irusta, I. Salinas, M.P. Pina, An optochemical humidity sensor based on immobilized Nile red in Y zeolite, Ind. Eng. Chem. Res. 46 (2007) 2335–2341.
[13] S. Sohrabnezhad, A. Pourahmad, M.A. Sadjadi, New methylene blue incorporated in mordenite zeolite as humidity sensor material, Mater. Lett. 61 (2007) 2311–2314.
[14] M. Osada, I. Sasaki, M. Nishioka, M. Sadakata, T. Okubo, Synthesis of a faujasite thin layer and its application for SO_2 sensing at elevated temperatures, Microporous Mesoporous Mater 23 (1998) 287–294.
[15] Z.B. Wang, H.T. Wang, A. Mitra, L.M. Huang, Y.S. Yan, Pure-silica zeolite low-*k* dielectric thin films, Adv. Mater 13 (2001) 746–749.
[16] S. Li, Z.J. Li, D. Medina, C. Lew, Y.S. Yan, Organic-functionalized pure-silica-zeolite MFI low-*k* films, Chem. Mater 17 (2005) 1851–1854.
[17] A. Mitra, T.G. Cao, H.T. Wang, Z.B. Wang, L.M. Huang, S. Li, Z.J. Li, Y.S. Yan, Synthesis and evaluation of pure-silica-zeolite BEA as low dielectric constant material for microprocessors, Ind. Eng. Chem. Res. 43 (2004) 2946–2949.
[18] Y. Liu, M. Sun, C.M. Lew, J. Wang, Y. Yan, MEL-type pure-silica zeolite nanocrystals prepared by an evaporation-assisted two-stage synthesis method as ultra-low-*k* materials, Adv. Funct. Mater 18 (2008) 1732–1738.
[19] H.K. Hunt, C.M. Lew, M. Sun, Y. Yan, M.E. Davis, Pure-silica LTA, CHA, STT, ITW, and -SVR thin films and powders for low-*k* applications, Microporous Mesoporous Mater 130 (2010) 49–55.
[20] C. Feng, K.C. Khulbe, T. Matsuura, R. Farnood, A.F. Ismail, Recent progress in zeolite/zeotype membranes, J. Membr. Sci. Res. 1 (2015) 49–72.
[21] R. Dragomirova, S. Wohlrab, Zeolite membranes in catalysis—from separate units to particle coatings, Catalysts 5 (2015) 2161–2222.
[22] N. Rangnekar, N. Mittal, B. Elyassi, J. Caro, M. Tsapatsis, Zeolite membranes—a review and comparison with MOFs, Chem. Soc. Rev. 44 (2015) 7128–7154.
[23] Y.S. Yan, M.E. Davis, G.R. Gavalas, Preparation of zeolite ZSM-5 membranes by in-situ crystallization on porous alpha-Al_2O_3, Ind. Eng. Chem. Res. 34 (1995) 1652–1661.
[24] V.A. Tuan, S.G. Li, J.L. Falconer, R.D. Noble, In situ crystallization of beta zeolite membranes and their permeation and separation properties, Chem. Mater. 14 (2002) 489–492.
[25] Z.B. Wang, Y.S. Yan, Controlling crystal orientation in zeolite MFI thin films by direct in situ crystallization, Chem. Mater 13 (2001) 1101–1107.
[26] J. Cejka, H. van Bekkum, A. Corma, F. Schueth, Introduction to Zeolite Science and Practice, third ed., Elsevier, New York, 2007.
[27] G. Xomeritakis, A. Gouzinis, S. Nair, T. Okubo, M.Y. He, R.M. Overney, M. Tsapatsis, Growth, microstructure, and permeation properties of supported zeolite (MFI) films and membranes prepared by secondary growth, Chem. Eng. Sci. 54 (1999) 3521–3531.
[28] M.P. Bernal, G. Xomeritakis, M. Tsapatsis, Tubular MFI zeolite membranes made by secondary (seeded) growth, Catal. Today 67 (2001) 101–107.
[29] M. Pan, Y.S. Lin, Template-free secondary growth synthesis of MFI type zeolite membranes, Microporous Mesoporous Mater 43 (2001) 319–327.
[30] W.Y. Xu, J.X. Dong, J.P. Li, J.Q. Li, F. Wu, A novel method for the preparation of zeolite ZSM-5, J. Chem. Soc. Chem. Commun. (1990) 755–756.
[31] T. Matsufuji, N. Nishiyama, K. Ueyama, M. Matsukata, Permeation characteristics of butane isomers through MFI-type zeolitic membranes, Catal. Today 56 (2000) 265–273.
[32] S. Alfaro, M. Arruebo, J. Coronas, M. Menendez, J. Santamaria, Preparation of MFI type tubular membranes by steam-assisted crystallization, Microporous Mesoporous Mater 50 (2001) 195–200.
[33] H.-Y. Lu, C.-H. Kung, B.-Z. Wan, Crystallinity control of zeolite nanoparticles for the preparation of mesoporous low-*k* films through a fast hydrothermal process, J. Taiwan Inst. Chem. Eng. 43 (2012) 971–979.
[34] H.Y. Lu, C.L. Teng, C.W. Yu, Y.C. Liu, B.Z. Wan, Addition of surfactant Tween 80 in coating solutions for making mesoporous pure silica zeolite MFI low-*k* films, Ind. Eng. Chem. Res. 49 (2010) 6279–6286.
[35] S. Mintova, T. Bein, Microporous films prepared by spin-coating stable colloidal suspensions of zeolites, Adv. Mater 13 (2001) 1880–1883.
[36] A.M. Doyle, G. Rupprechter, N. Pfänder, R. Schlögl, C.E.A. Kirschhock, J.A. Martens, H.J. Freund, Ultra-thin zeolite films prepared by spin-coating Silicalite-1 precursor solutions, Chem. Phys. Lett. 382 (2003) 404–409.
[37] C.M. Lew, Z. Li, S. Li, S.-J. Hwang, Y. Liu, D.I. Medina, M. Sun, J. Wang, M.E. Davis, Y. Yan, Pure-silica-zeolite MFI and MEL low-dielectric-constant films with fluoro-organic functionalization, Adv. Funct. Mater 18 (2008) 3454–3460.
[38] Z.J. Li, C.M. Lew, S. Li, D.I. Medina, Y.S. Yan, Pure-silica-zeolite MEL low-k films from nanoparticle suspensions, J. Phys. Chem. B 109 (2005) 8652–8658.
[39] S. Mintova, M. Reinelt, T.H. Metzger, J. Senker, T. Bein, Pure silica BETA colloidal zeolite assembled in thin films, Chem. Commun. (2003) 326–327.
[40] M. Vilaseca, S. Mintova, K. Karaghiosoff, T.H. Metzger, T. Bein, $AlPO_4$-18 synthesized from colloidal precursors and its use for the preparation of thin films, Appl. Surf. Sci. 226 (2004) 1–6.
[41] J.A. Lee, L. Meng, D.J. Norris, L.E. Scriven, M. Tsapatsis, Colloidal crystal layers of hexagonal nanoplates by convective assembly, Langmuir 22 (2006) 5217–5219.
[42] M.X. Xu, Y. He, Y.P. Wang, X.M. Cui, Preparation of a non-hydrothermal NaA zeolite membrane and defect elimination by vacuum-inhalation repair method, Chem. Eng. Sci. 158 (2017) 117–123.
[43] A.E.W. Beers, T.A. Nijhuis, N. Aalders, F. Kapteijn, J.A. Moulijn, BEA coating of structured supports—performance in acylation, Appl. Catal. A 243 (2003) 237–250.
[44] M.V. Landau, D. Tavor, O. Regev, M.L. Kaliya, M. Herskowitz, V. Valtchev, S. Mintova, Colloidal nanocrystals of zeolite beta stabilized in alumina matrix, Chem. Mater 11 (1999) 2030–2037.
[45] K.A. Sashkina, Z. Qi, W. Wu, A.B. Ayupov, A.I. Lysikov, E.V. Parkhomchuk, The effect of H_2O/SiO_2 ratio in precursor solution on the crystal size and morphology of zeolite ZSM-5, Microporous Mesoporous Mater 244 (2017) 93–100.
[46] T. Kuzniatsova, Y. Kim, K. Shqau, P.K. Dutta, H. Verweij, Zeta potential measurements of zeolite Y: application in homogeneous deposition of particle coatings, Microporous Mesoporous Mater 103 (2007) 102–107.

[47] R. Watanabe, T. Yokoi, T. Tatsumi, Synthesis and application of colloidal nanocrystals of the MFI-type zeolites, J. Colloid Interface Sci. 356 (2011) 434–441.
[48] J. Kobler, H. Abrevaya, S. Mintova, T. Bein, High-silica zeolite-BETA: from stable colloidal suspensions to thin films, J. Phys. Chem. C 112 (2008) 14274–14280.
[49] S. Kallus, J.M. Condre, A. Hahn, G. Golemme, C. Algieri, P. Dieudonné, P. Timmins, J.D.F. Ramsay, Colloidal zeolites and zeolite membranes, J. Mater. Chem. 12 (2002) 3343–3350.
[50] B.J. Schoeman, J. Sterte, Colloidal zeolite-preparation, properties and applications, KONA Powder Part. J. 15 (1997) 150–158.
[51] H.Y. Lu, C.L. Teng, C.H. Kung, B.Z. Wan, Preparing mesoporous low-k films with high mechanical strength from noncrystalline silica particles, Ind. Eng. Chem. Res. 50 (2011) 3265–3273.
[52] N. Kosinov, E.J.M. Hensen, Synthesis and separation properties of an α-alumina-supported high-silica MEL membrane, J. Membr. Sci. 447 (2013) 12–18.
[53] H. Awala, J.P. Gilson, R. Retoux, P. Boullay, J.M. Goupil, V. Valtchev, S. Mintova, Template-free nanosized faujasite-type zeolites, Nat. Mater 14 (2015) 447–451.
[54] Y.H. Wen, P.C. Lin, C.C. Hua, S.A. Chen, Dynamic structure factor for large aggregate clusters with internal motions: a self-consistent light-scattering study on conjugated polymer solutions, J. Phys. Chem. B 115 (2011) 14369–14380.
[55] R.H. Guo, C.H. Hsu, C.C. Hua, S.A. Chen, Colloidal aggregate and gel incubated by amorphous conjugated polymer in hybrid-solvent medium, J. Phys. Chem. B 119 (2015) 3320–3331.
[56] A. Siegert, Radiation Laboratory Report No. 475, Massachusetts Institute of Technology, Cambridge, Massachusetts, 1943.
[57] S.W. Provencher, A constrained regularization method for inverting data represented by linear algebraic or integral equations, Comput. Phys. Commun. 27 (1982) 213–227.
[58] D.E. Koppel, Analysis of macromolecular polydispersity in intensity correlation spectroscopy: the method of cumulants, J. Chem. Phys. 57 (1972) 4814–4820.
[59] B.J. Berne, R. Pecora, Dynamic Light Scattering: with Applications to Chemistry, Biology, and Physics, Dover Publications, New York, 2000.
[60] L.R. Follens, A. Aerts, M. Haouas, T.P. Caremans, B. Loppinet, B. Goderis, J. Vermant, F. Taulelle, J.A. Martens, C.E. Kirschhock, Characterization of nanoparticles in diluted clear solutions for Silicalite-1 zeolite synthesis using liquid 29Si NMR, SAXS and DLS, Phys. Chem. Chem. Phys. 10 (2008) 5574–5583.
[61] B.J. Schoeman, J. Sterte, J.E. Otterstedt, Dynamic light scattering applied to the synthesis of colloidal zeolite, J. Porous Mater 1 (1995) 185–198.
[62] A. Aerts, L.R.A. Follens, M. Haouas, T.P. Caremans, M.A. Delsuc, B. Loppinet, J. Vermant, B. Goderis, F. Taulelle, J.A. Martens, C.E.A. Kirschhock, Combined NMR, SAXS, and DLS study of concentrated clear solutions used in silicalite-1 zeolite synthesis, Chem. Mater 19 (2007) 3448–3454.
[63] L. Dimitrov, V. Valtchev, D. Nihtianova, Y. Kalvachev, Submicrometer zeolite a crystals formation: low-temperature crystallization versus vapor phase gel transformation, Cryst. Growth Des. 11 (2011) 4958–4962.
[64] N. Kosinov, V.G.P. Sripathi, E.J.M. Hensen, Improving separation performance of high-silica zeolite membranes by surface modification with triethoxy-fluorosilane, Microporous Mesoporous Mater 194 (2014) 24–30.
[65] O. Larlus, S. Mintova, T. Bein, Environmental syntheses of nanosized zeolites with high yield and monomodal particle size distribution, Microporous Mesoporous Mater 96 (2006) 405–412.
[66] H.L. Chang, W.H. Shih, A general method for the conversion of fly ash into zeolites as ion exchangers for Cesium, Ind. Eng. Chem. Res. 37 (1998) 71–78.
[67] C. Abrioux, B. Coasne, G. Maurin, F. Henn, M. Jeffroy, A. Boutin, Cation behavior in faujasite zeolites upon water adsorption: a combination of Monte Carlo and molecular dynamics simulations, J. Phys. Chem. C 113 (2009) 10696–10705.
[68] K. Shirono, A. Endo, H. Daiguji, Molecular dynamics study of hydrated faujasite-type zeolites, J. Phys. Chem. B 109 (2005) 3446–3453.
[69] J. Jänchen, H. Stach, U. Hellwig, Water sorption in faujasite and chabazite type zeolites of varying lattice composition for heat storage applications, Stud. Surf. Sci. Catal. 174 (2008) 599–602.
[70] A.C. Yang, Y.S. Li, C.H. Lam, H.Y. Chi, I.C. Cheng, D.Y. Kang, Solution-processed ultra-low-k thin films comprising single-walled aluminosilicate nanotubes, Nanoscale 8 (2016) 17427–17432.
[71] M. Oh, Y. Kim, J. Park, Factors affecting the complex permittivity spectrum of soil at a low frequency range of 1 kHz–10 MHz, Environ. Geol. 51 (2006) 821–833.
[72] D. Shamiryan, T. Abell, F. Iacopi, K. Maex, Low-k dielectric materials, Mater. Today 7 (2004) 34–39.
[73] E. Izci, A. Izci, Dielectric behavior of the catalyst zeolite NaY, Turk. J. Chem. 31 (2007) 523–530.
[74] A.C. Lopes, C.M. Costa, R.S.i. Serra, I.C. Neves, J.L.G. Ribelles, S. Lanceros-Méndez, Dielectric relaxation, ac conductivity and electric modulus in poly(-vinylidene fluoride)/NaY zeolite composites, Solid State Ionics 235 (2013) 42–50.